Influence of the internal flow conditions of slit nozzles on the stability of liquid sheets: Experimental results

Jochen Scholz, Karsten Roetmann, Volker Beushausen

Laser-Laboratorium Goettingen e.V., Hans-Adolf-Krebs-Weg 1, D-37077Goettingen, Germany, Phone: +49 551 5035 23, e-mail: Jochen.Scholz@llg.gwdg.de

This work focuses on the interconnection of internal flow field and liquid sheet stability of slit nozzles. The main issue was to supplement the existing experimental data with particle image velocimetry (PIV) experiments on the inner flow field of three different nozzle designs and visualization of the sheet modulation and breakup at Reynolds numbers about *Re*=19000. The main difference of these nozzles was the channel length. Like in former investigations, the dominating influence of the internal flow conditions on the film stability became obvious. The results support the conclusion that a certain amount of turbulence stabilizes the liquid film, as stated by [2]. The use of a double pulse technique for backlit photography of the free liquid film gave the opportunity to determine the velocity of the surface deformations near the nozzle exit. This in combination with the knowledge about the internal flow field allowed drawing conclusions about the energy transfer between core flow and free liquid surface at the nozzle exit. It is suggested that this energy transfer plays an important roll in the promotion of disturbances and surface deformation and therefore has an essential influence on the liquid sheet stability.

1. Introduction

Atomization of liquids is of great scientific and industrial interest and in order to control or model atomization it is necessary to understand the breakup phenomena. In addition to breakup mechanisms of liquid jets, the disintegration processes of liquid sheets have been extensively studied in the past decades. In the most recent studies [1, 2, 3, 4] the consideration of the internal flow field of the nozzle was included into the investigation of liquid sheet disintegration. In these studies the important influence of the inner flow field on the modulation of the liquid film became quite evident but there is still a lack of experimental data to understand the disintegration processes. Furthermore, a broad base of experimental data is needed to serve as input or validation of numerical simulations.
Subsequent to our recent work [3], the present work focuses on the interconnection of internal flow field and liquid sheet stability. The main issue is to supplement the existing experimental data with particle image velocimetry (PIV) experiments on the internal flow field of different nozzle designs and visualization of the sheet modulation and breakup at higher Reynolds numbers (up to *Re*=23400). PIV experiments are carried out at the exit of three nozzles with different channel lengths giving snapshots of the instantaneous flow field as well as time averaged velocity profiles of the main velocity component in stream wise direction (u) and profiles of its fluctuations (u'). The free liquid sheet is observed by backlit photography whereas a double pulse technique is used. This gives the possibility to examine the velocity of the surface waves near the nozzle exit.

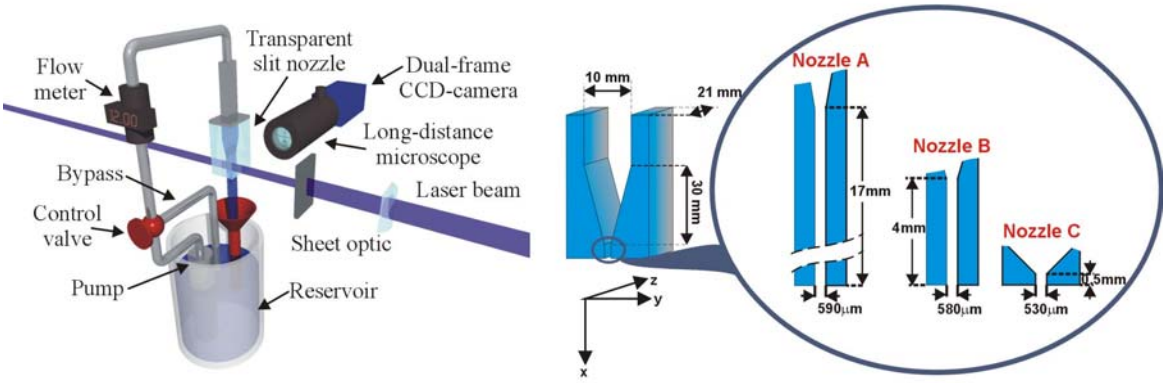

Fig. 1 Experimental setup for PIV investigations (left) and examined nozzle designs (right).

2. PIV Investigations of internal nozzle flows

The left side of figure 1 shows the experimental setup for PIV investigations schematically. It is quite similar with that used in [3], but a more powerful pump, tubes and valves with higher flow rates were used to reach higher *Re* numbers. The liquid supply was provided by a fifteen-level rotary pump. The maximum counter-pressure was 10 bar. The flow through the nozzle was controlled by a valve and a bypass and it was measured by a flow meter. The replaceable transparent nozzle (description see below) was mounted at the end of a 40 cm long calming channel and held by a micro positioning system. The free liquid stream was caught by a funnel and led back to the reservoir. Water, seeded with 1µm glass spheres as tracer particles was used as test fluid. Due to the heat loss of the pump the water was heated and after a certain operation time a quasi-statical temperature equilibrium was reached. The presented investigations were conducted at an equilibrium water temperature of 35±7 °C, which leads to a kinematic viscosity of $\nu=(0.73\pm0,13)\cdot10^{-6}$ m^2/s. This viscosity, the measured volume flux and the geometry of the nozzle channel were used to compute the *Re* number.
Figure 1 also sketches the optical setup of the PIV system. The collinearly overlapped beams of a double pulse excimer laser (Compex 150 Lambda Physik, wavelength 351 nm, pulse duration approx. 20 ns) were formed into a laser-sheet using cylindrical lenses and a slit aperture. Perpendicular to the light-sheet, the scattered light from the illuminated tracer particles was captured separately for both exposures by a dual-frame CCD-camera which was equipped with a long-distance microscope. The time delay between both exposures / frames could be set from 0.4 µs upwards, according to the actual velocity. A commercial PIV software (DaVis6.2, LaVision GmbH) was used to compute the velocity fields which resulted from each image pair by using standard cross-correlation PIV algorithms.
In this study, three different nozzle designs were used. They are sketched in the right part of figure 1. All nozzles were made of synthetic quartz glass. Except of the nozzle channel, the nozzle geometry was the same for nozzles A and B. The inlet was 10 mm high and 21 mm wide. The length of the contraction zone was 30 mm. The nozzle channel had a height of 590 µm (nozzle A) and 580 µm (nozzle B), respectively. The important difference between these two nozzles was the channel length of 17 mm for nozzle A and 4 mm for nozzle B. Nozzle C had the same inlet dimensions as nozzles A and B but nozzle C had a shorter contraction zone of 4.7 mm and a shorter channel length of approximately 0.5 mm. The channel height of 530 µm was comparable to that of nozzles A and B.
For each nozzle and each examined flow condition 80 to 100 single PIV measurements were conducted and snapshots of the instantaneous flow field were computed. These snapshots were averaged to a time averaged velocity field for each flow condition. In this averaging

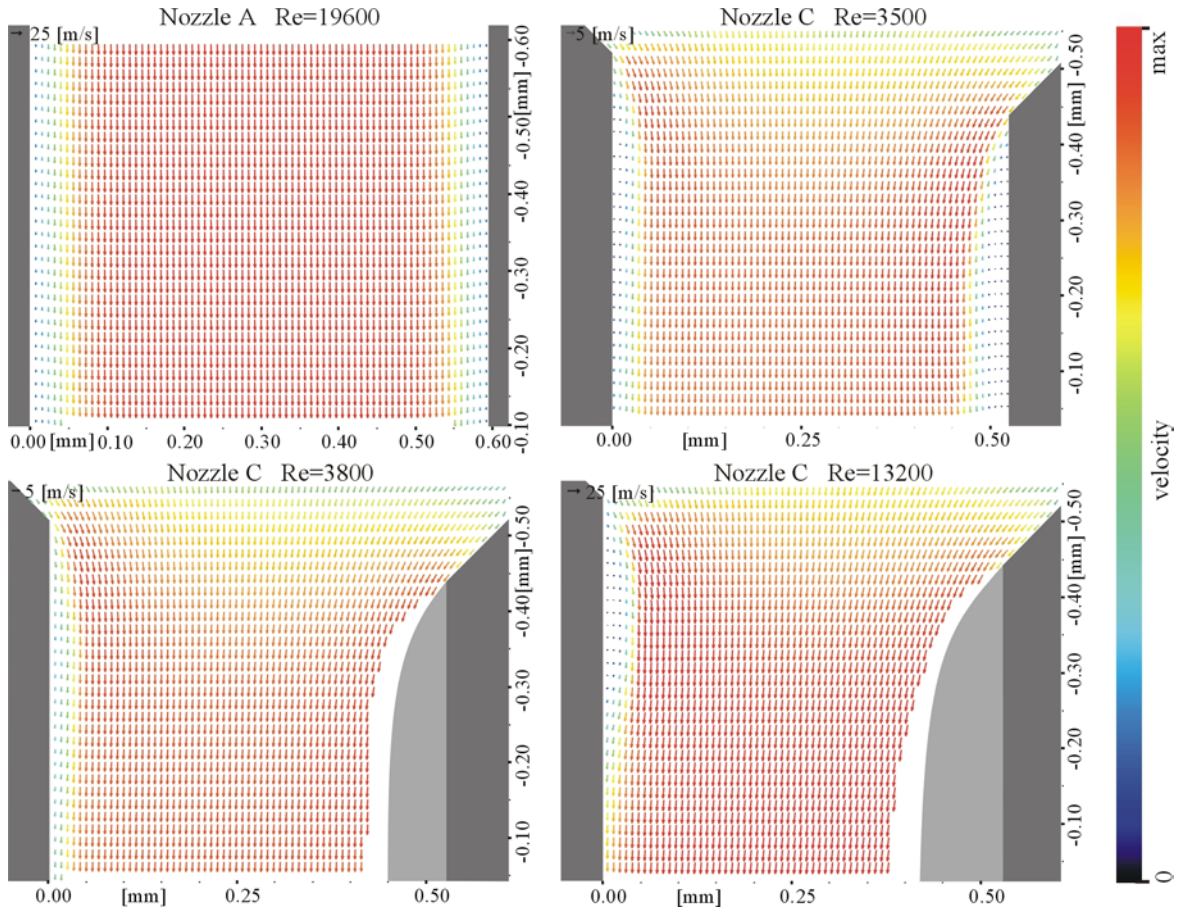

Fig. 2 Averaged velocity fields at the nozzle exit of nozzle A and C. The dark gray areas represent the nozzle walls, the light gray areas represent air flowed into the nozzle due to the separation of the liquid from the wall at higher *Re* numbers for nozzle C.

procedure the temporal fluctuations (i.e. the standard deviation) of the velocity is computed as well. For a better understanding and quantitative comparison, velocity profiles of the main stream wise velocity *u* and profiles of its fluctuation *u'* were taken near the nozzle exit (a detailed explanation of this data evaluation procedure can be found in [3]).

Figure 2 shows averaged velocity fields close to the exit of nozzle A and C. The velocity field of nozzle B looks qualitatively very similar to that of nozzle A, so it was left out in this example. In each flow field of figure 2 the main stream wise velocity is directed from top to bottom, the walls are denoted by the dark gray areas and the distance from the nozzle exit is indicated at the right wall. The velocity value is denoted by the length of the vector arrows and color coded from zero (black) to the maximum value (red) for each of the 4 examples differently. In the case of nozzle A (and therefore for B as well) the velocity field is very homogeneous in stream wise direction and it appears axially symmetric in respect to the center line. There is a velocity plateau in the center of the flow and the velocity decreases only near the walls. This picture of a partly developed and partly turbulent channel flow has been observed qualitatively for all examined flow conditions for nozzle A and B. For nozzle C the situation is different. Here, the end of the contraction zone is very close to the nozzle exit and has therefore a dominating influence. Due to limited fabrication accuracy both channel walls have slightly different lengths (approx. 75 µm, see figure 2). So the flow field is not axially symmetric. (Nevertheless, this nozzle has been investigated because technical nozzle flows are asymmetric in many cases as well.) At lower *Re* numbers (*Re*=3500) the flow separates from the walls on both sides at the end of the contraction zone. At the left wall

the flow starts to reattach to the wall further downstream whereas the dead water extends up to the nozzle exit at the right wall. At higher flow velocities (*Re*=3800) the nozzle "flips" and the liquid separates completely from the right nozzle wall. The light gray areas in figure 2 for nozzle C at *Re*=3800 and *Re*=13200 represent the air flowed into the nozzle and show the position of the liquid surface. Due to surface reflections, it was not possible to measure the flow field very close to the liquid surface so there are blank areas in figure 2. At the left wall at *Re*=3800 the separated flow reattaches further downstream building a separation bubble. This separation bubble contracts and becomes even more pronounced at higher *Re* numbers as can be seen at *Re*=13200 in figure 2. Here, the boundary region directly at the nozzle exit is smaller and the velocity gradient is steeper as in the case of lower *Re* numbers. At even higher *Re* numbers (*Re*=18400, not shown here) cavitation occurs and the separation bubble converts into a cavitation bubble which seems to be wider expanded than the separation bubble. So the boundary region in the wake of this bubble is slightly broadened as well.

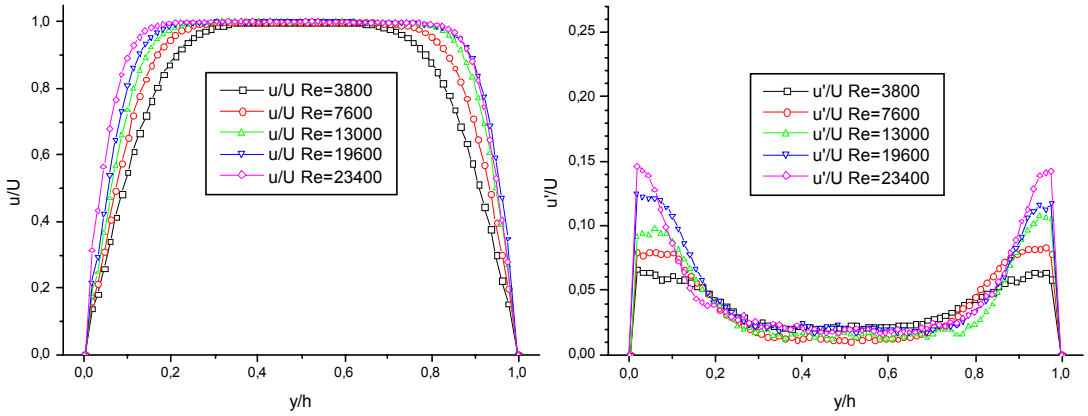

Fig. 3 Velocity profiles (left) and fluctuations (right) for nozzle A.

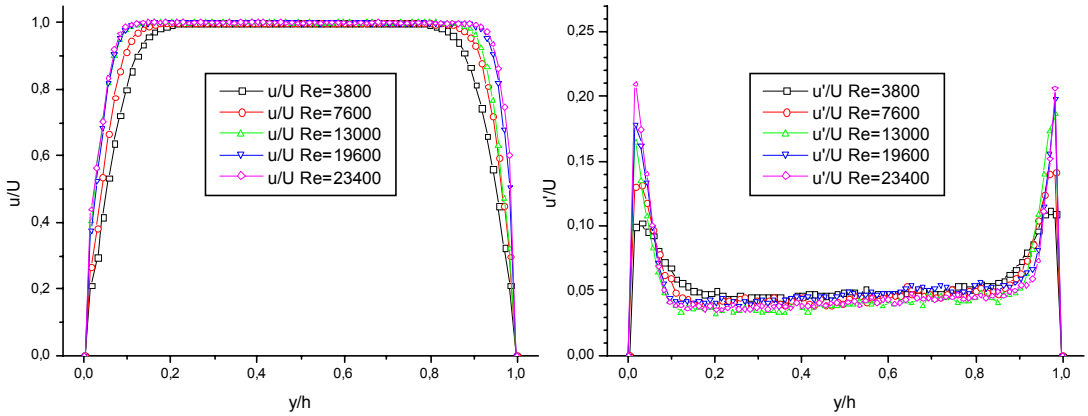

Fig. 4 Velocity profiles (left) and fluctuations (right) for nozzle B.

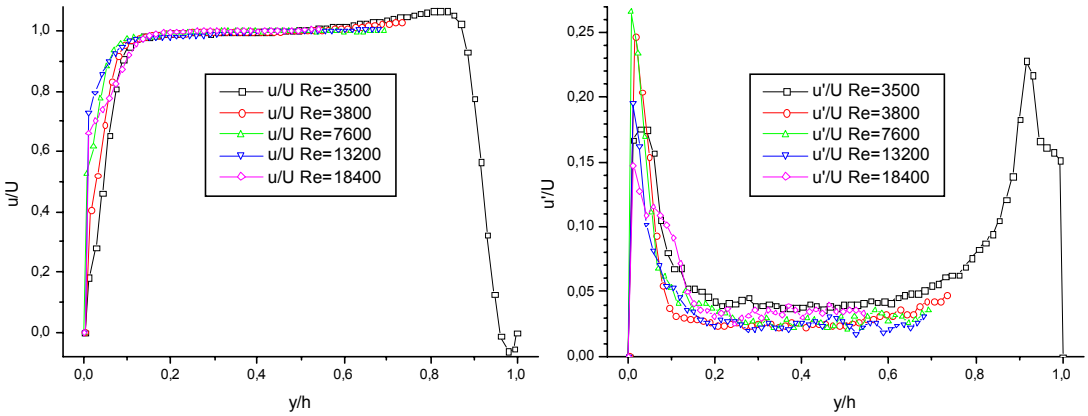

Fig. 5 Velocity profiles (left) and fluctuations (right) for nozzle C.

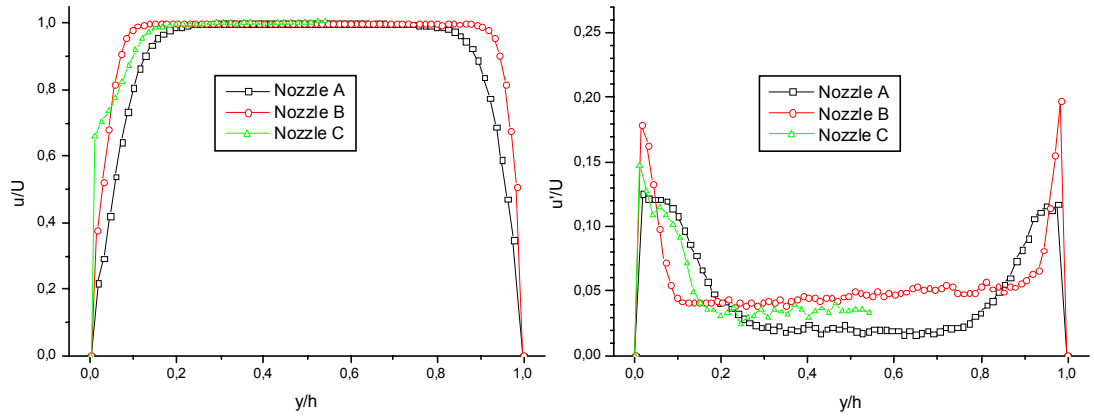

Fig. 6 Comparison of the velocity profiles (left) and fluctuations (right) for the different nozzles. Nozzle A and B: *Re*=19600, nozzle C: *Re*=18400.

More detailed information about the flow conditions at the nozzle exit of nozzle A, B and C can be drawn from the velocity profiles. Figures 3 to 5 show the profiles of the main stream wise velocity component *u* near the nozzle exit normalized with the centerline velocity *U* and its corresponding normalized temporal standard deviation *u'/U* for the three nozzles at different *Re* numbers. In the case of the homogeneous fields of nozzles A and B these profiles were taken in a range of 400 µm starting 150 µm upstream of the nozzle exit. In the case of nozzle C the range for the profiles begins 70 µm upstream of the nozzle exit and is 30 µm to 100 µm long, depending on the homogeneity of the vector field. Like in former investigations [3], figures 3 and 4 show for nozzles A and B that the velocity profile flanks get steeper with increasing *Re* number whereas the velocity plateau gets wider. The corresponding fluctuation profiles show that the fluctuations near the walls increase as well with increasing *Re* number, building a turbulent boundary layer. The difference between these two nozzles of different lenght is the dimension of the boundary layer, as compared in figure 6. In the case of the longer nozzle A the fluctuations spread out more towards the center of the flow than in the case of the shorter nozzle B. This is in good agreement with our former results [3] and shows that the turbulent boundary layer grows along the channel length. This wider turbulent boundary layer may explain as well the fact, that the velocity profile of nozzle A is not as steep as the profile of nozzle B at the same *Re* number in figure 6.

A slightly different situation can be observed in the case of the velocity profiles of nozzle C in figure 5. As mentioned above, velocity measurements at the right wall were only possible at the lowest investigated *Re* number. Here, the asymmetry of the nozzle becomes obvious in the asymmetry of the profiles. At *Re*=3500 even a recirculation area with negative stream wise velocity can be observed near the right wall. Like in the case of nozzles A and B, the velocity profiles of nozzle C at the left wall get steeper with increasing *Re* number, with the exception of the step between *Re*=13200 and *Re*=18400 where the transition to cavitation occurs. But in this case the above mentioned deformation of the separation bubble should be responsible, rather than the development of a turbulent boundary layer. This is supported by the corresponding fluctuation profiles. They show increasing fluctuations from *Re*=3500 to *Re*=7600. But at higher *Re* numbers the fluctuations decrease again when the flow reattaches the wall.

A comparison between nozzle C and nozzles A and B in figure 6 shows that the velocity gradient directly at the wall of nozzle C is the steepest although the fluctuation profile is wider than in the case of nozzle B. This may be due to a reattached flow with no grown boundary layer but with fluctuations in the wake of the cavitation bubble caused by fluctuation of the cavitation itself, which occurs at this high Re numbers.

3. Investigations of the free liquid film

The free liquid film was observed by double-pulse backlit photography. The above mentioned double-pulse excimer-laser was used as light source and a double-pulse CCD-camera was used to get pairs of backlit photographs with defined temporal delay. So, it was possible to follow the movement of surface waves and to determine their velocity. Figure 7 gives an overview of the free liquid surface stability of the three nozzles at comparable *Re* numbers of *Re*=19600 for nozzles A and B and *Re*=18400 for nozzle C, respectively. Each free film image consists of 4 single backlit photographs at different positions downstream of the nozzle exit. The views through the liquid film in the left part of figure 7 show that the free liquid sheets of nozzles A and B are contracted from nozzle exit to the bottom, forced by the surface tension. This contraction, which is most pronounced in the case of nozzle B, indicates an almost intact liquid surface. The contraction can be seen at nozzle C to a certain extent as well. But at least 250 mm downstream from the nozzle the liquid film is disrupted by the first holes and the disruption increases further downstream. While the film of nozzle A is the most nontransparent one, the liquid film of nozzle B appears to be the most stable one. The side view of the free streams in the right part of figure 7 is influenced by the rim of the film. Nevertheless the side view shows that in the case of nozzle A small droplets start to detach from the liquid surface less than 20 mm from the nozzle exit. The droplet fan covers the wavy but intact liquid surface further downstream. These droplets are mainly responsible for the nontransparent appearance of the view through the film. About 300 mm to 350 mm downstream of nozzle A, bigger irregular waves grow, leading to bursting bags of the liquid film. This produces ligaments of different shape and size. In the case of nozzle B only very small droplets become obvious in the side view and the growth of bigger waves occur further downstream than in the case of nozzle A. At nozzle B the waves seem to be dominated by the rims of the film. Here, no disruption of the liquid surface can be observed. In the case of nozzle C there are no droplets visible in the side view at all. But here, the growth of bigger waves starts closer towards the nozzle exit and first ligaments detaching from the liquid surface can be observed about 250 mm downstream of the nozzle exit. This disruption of the liquid surface, forced by aerodynamic interaction, increases further downstream similar to the situation in the corresponding view through the film.

Figure 8 gives more detailed backlit views through the film at different positions downstream of the nozzle exits. Directly at the nozzle exit, nozzles A and B show a quite smooth liquid surface. About 1 mm below the exit, surface waves are grown to an extent that they are clearly visible. The wave growth continues for approximately 1 mm until an irregularly roughened nearly nontransparent surface is formed. As seen in the side view of figure 7 droplets detach from these roughened film surfaces of nozzle A and B. These droplets can be seen in figure 8 in the detailed picture 44 mm below the nozzle exits. Although the droplets of irregular size are much smaller and less for nozzle B than in the case of nozzle A, they are clearly visible. Behind the droplets the roughness of the intact liquid surface smoothes due to surface tension forces. This smoothing becomes more obvious in comparison with the situation about 93 mm below the nozzle exits of nozzles A and B. Here, the droplets can be seen in front of an even smoother liquid surface. The comparison of these first two nozzles in figure 8 shows that all structures, the wavelengths and the droplets are bigger and more pronounced at the free film of the longer nozzle A than in the case of nozzle B. Again the situation is slightly different for nozzle C in figure 8. Here, the irregular roughness of the surface starts directly at the nozzle exit without wave growth on a smooth area. On the other hand, this roughness starts to smooth by surface tension within the first 4 mm below the nozzle exit. In the picture 44 mm further downstream, only very few very small droplets can

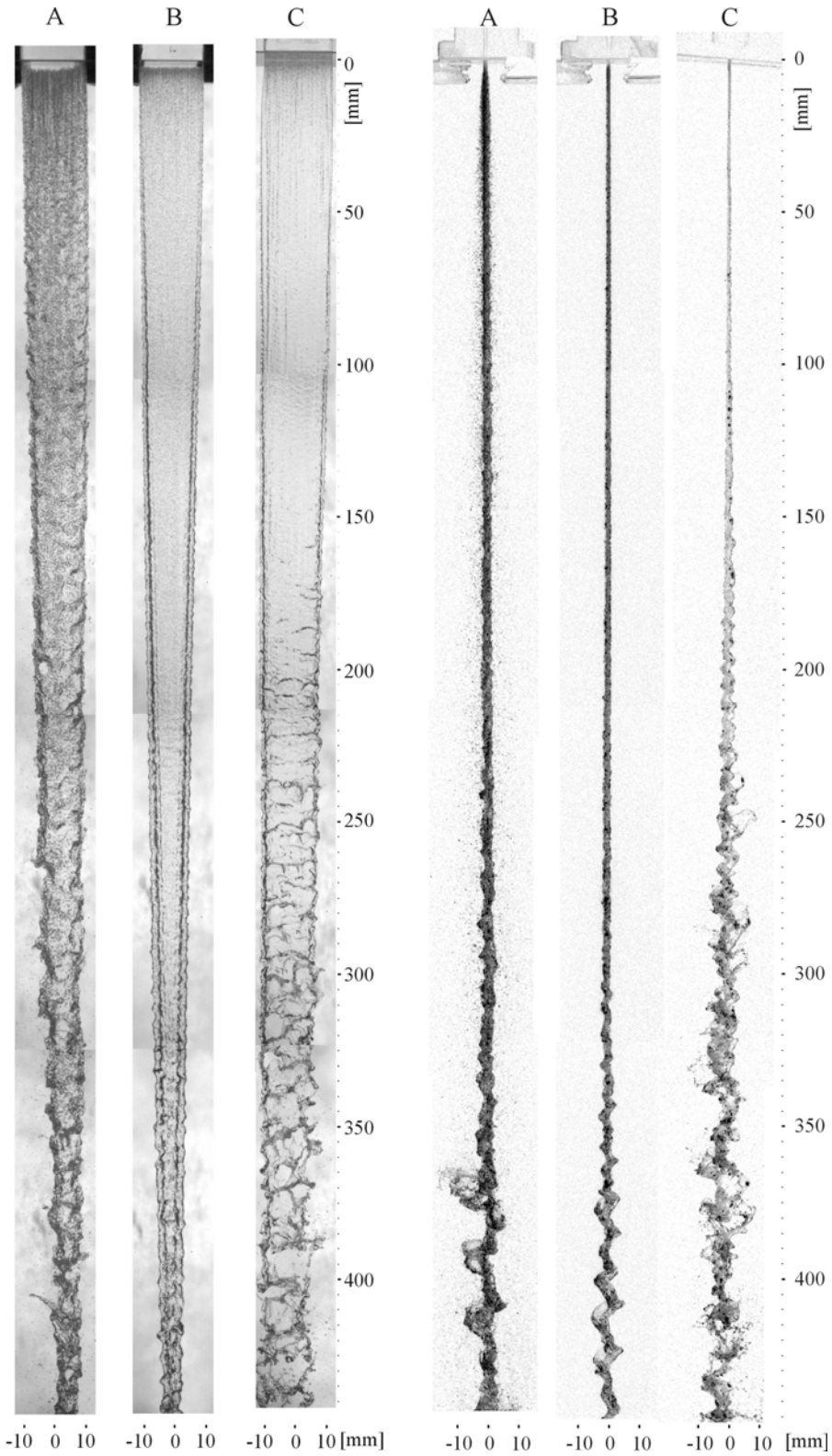

Fig. 7 Backlit photographs of the free liquid films of nozzle A, B (*Re*=19600) and C (*Re*=18400). View through the film (left) and side view (right).

be observed in front of a liquid surface that appears to be smoother than in the case of nozzles A and B at the corresponding position.

Another difference can be seen from the velocity profiles of the surface structures along the free liquid films in figure 9. These profiles show the energy transfer from the core flow

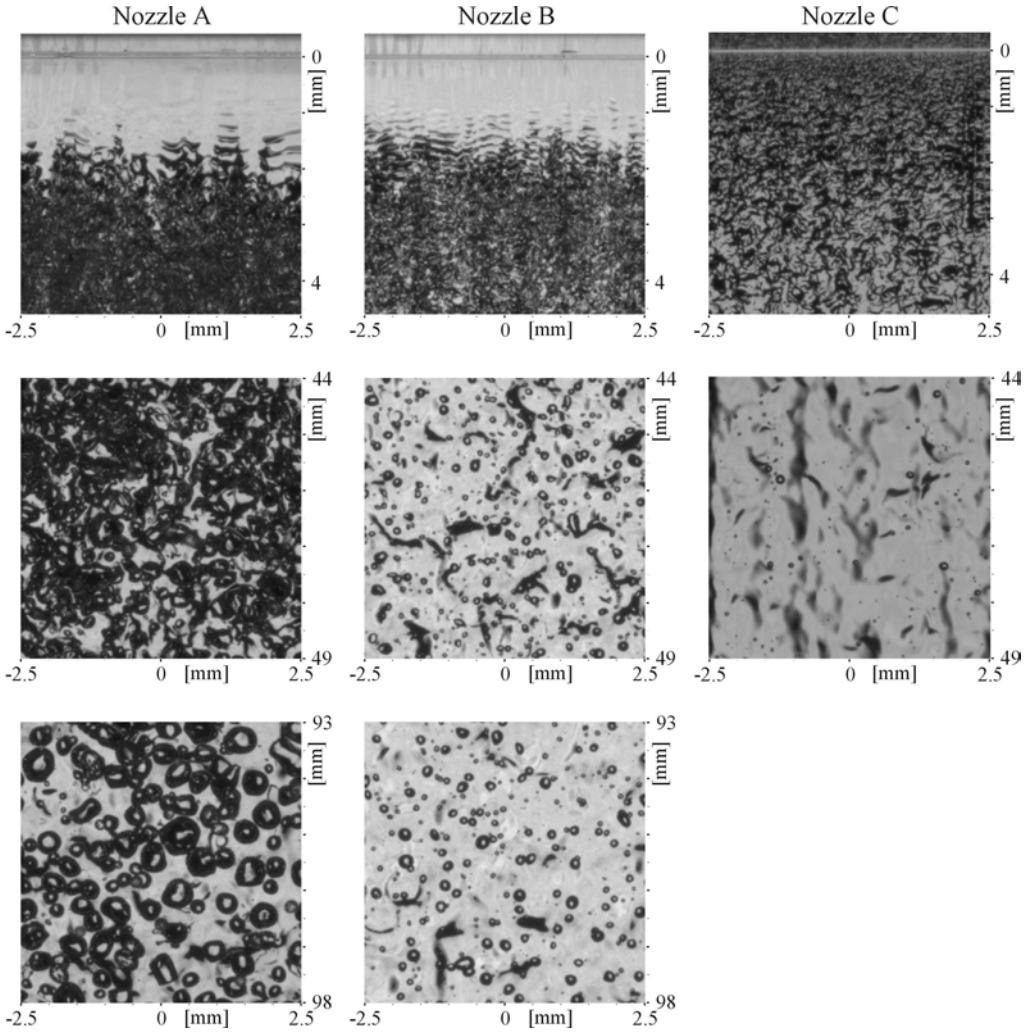

Fig. 8 Detailed backlit views through the free liquid films of nozzle A, B (*Re*=19600) and C (*Re*=18400) at different positions downstream of the nozzle exit.

towards the liquid surface of the free film. They were gained by detailed backlit photographs (like those in figure 8) using the above mentioned double pulse technique and PIV algorithms for velocity determination. Figure 9 shows for all nozzles that the velocity of the surface structures increases from zero at the nozzle exit to a maximum value which is reached approximately 20 mm further downstream. But obviously, the velocity increase directly at the nozzle exit is much faster for nozzle C than in the cases of nozzles A and B. The increase of the profile for nozzle B directly at the nozzle exit is again steeper than that for nozzle A.

This may be explained by the different velocity gradients of the internal nozzle flow near the walls, as can be seen in figure 6. Nozzle C has the steepest velocity gradient directly at the left wall in figure 6. So at the nozzle exit, where the wall adhesion ends, the energy or velocity transfer from the inner part of the flow toward the surface can take place over a short distance resulting in a fast acceleration of the surface. The next steepest velocity gradient near the wall is that of nozzle B and the less steep that of nozzle A in figure 6. This is corresponding to the ranking of the surface structure acceleration on the free films in figure 9. Furthermore, nozzle A with the lowest acceleration and the widest boundary layer show in figure 8 the growth of the most pronounced surface waves detaching the biggest droplets while nozzle C with the highest acceleration produces the smoothest liquid surface and the smallest droplets down to 50 mm below nozzle exit. This means, the energy transfer seems to promote surface disturbances near the nozzle exit.

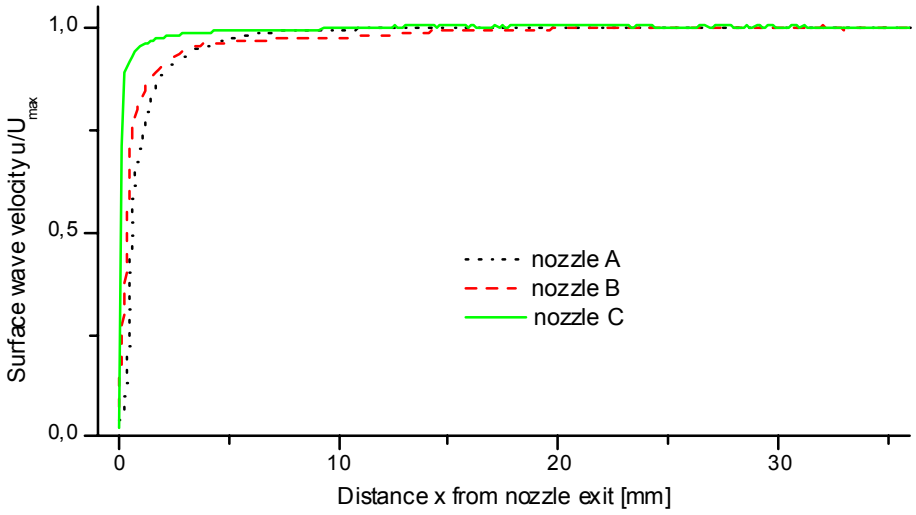

Fig. 9 Surface wave velocity of the free films of nozzle A, B (*Re*=19600) and C (*Re*=18400).

4. Conclusions

The experimental results of this study confirm conclusions of former work and bring up new aspects about the interconnection between internal nozzle flow and liquid film stability. The development of turbulent boundary layers stabilizes the liquid film of nozzle A and B as long as the turbulence is not too strong, like stated in [2]. On the other hand, the broadened boundary layer of nozzle A causes a more pronounced roughness of the surface leading to more and bigger droplets detaching from the surface. It is suggested that the energy transfer or velocity equalization between core flow and liquid surface at the nozzle exit plays an important roll in the promotion of these disturbances. The co-flow of the droplets itself may protect the intact surface from further aerodynamic disruption to a certain extent. In the case of nozzle C no turbulent boundary layer is developed. Anyhow, the separation bubble respectively the cavitation bubble creates fluctuations that cause the liquid surface to roughen directly at the nozzle exit. But these disturbances are too week. Furthermore, the velocity equalization between core flow and surface is very quick due to the steep velocity gradient of the internal flow of nozzle C. So the disturbances are not promoted by velocity transfer and the roughness is smoothed by surface tension. In the end, the free film of nozzle C disrupts mainly by aerodynamic interaction. This is another indication for the important influence of internal nozzle flow on liquid sheet stability. These experimental results supplement the existing database and can serve for a comparison with numerical results of other groups.

5. References

[1] Heukelbach K.; Tropea C. 2001 *Influence of the inner flowfield of flat fan pressure atomizers on the disintegration of the liquid sheet*, ILASS-Europe 2001, Zurich

[2] Heukelbach K., Jakirlic S., Nakic R., Tropea C. 2002 *Influence of turbulence on the stability of liquid sheets*, ILASS-Europe 2002, Zaragoza

[3] Scholz J., Roetmann K., Beushausen V. 2002 *PIV-Investigations of internal slit nozzle flows and their influence on liquid sheet breakup*, ILASS-Europe 2002, Zaragoza

[4] Klein M. 2003 *Direkte Numerische Simulation des primären Strahlzerfalls in Einstoffzerstäuberdüsen*, Fortschr.-Ber. VDI Reihe 7 Nr. 445, VDI Verlag Düsseldorf